ADVANCES IN ATMOSPHERIC SCIENCES, VOL. 24, NO. 4, 2007, 619–630

A Simple but Accurate Ultraviolet Limb-Scan Spherically-Layered Radiative-Transfer-Model Based on Single-Scattering Physics

GUO Xia*[1] (郭 霞), LÜ Daren[1] (吕达仁), and LÜ Yao[2] (吕 曜)

[1] *Institute of Atmospheric Physics, Chinese Academy of Sciences, Beijing* 100029

[2] *Institute of Electronics, Chinese Academy of Sciences, Beijing* 100008

(Received 30 June 2006; revised 14 October 2006)

ABSTRACT

Here we present a study focusing on atmospheric limb-scattered radiative characteristics in the ultraviolet band by using a limb-scan spherically-layered radiative-transfer-model based on the single-scattering approximation, which was developed by the present authors. We have applied an accurate numerical integration technique involving an auto-adaptive modified-space step, which assured high accuracy and simplification. Comparisons were made to the newly released spherical radiative transfer model, SCIATRAN2.0, which was developed by Institute of Remote Sensing/Institute of Environmental Physics (IUP/IFE) at University of Bremen and to measurements collected via an ultraviolet spectrometer on the Solar Mesospheric Explorer (SME) satellite, which was launched in October, 1981. Preliminary results indicate that the present model provides a good interpretation of the earth-limb scattered ultraviolet radiance, and thus, is suitable for the study of the ultraviolet-limb radiative-transfer problem with high accuracy.

Key words: ultraviolet, limb geometry, spherical atmosphere, radiative-transfer model

DOI: 10.1007/s00376-007-0619-3

1. Introduction

In recent years, significant changes in the composition and behavior of the Earth's atmosphere have been reported, including the ozone loss in the stratosphere in the Arctic and Antarctic regions (Newman et al., 1997; Müller et al., 1997), the global increase of the tropospheric ozone along with the increase in tropospheric "greenhouse" gases such as CO_2, CH_4, and N_2O. In order to study these changes along with their induced environmental and climatological problems, knowledge of both global and long-term distributions and changes of the atmospheric constituents is essential.

Remote sensing of the Earth's atmosphere in the UV-Vis spectral region by means of ground-based and space-borne instruments can yield important information on the temporal and spatial behavior of several atmospheric constituents such as trace gases, aerosols, clouds and air density on a global scale. The abundance and vertical distributions of atmospheric trace gases in the stratosphere and the troposphere, as well as the stratospheric-tropospheric exchange, can be investigated by using measurements by the Solar Backscatter Ultraviolet (SBUV) spectrometer (Heath et al., 1975; Fleig et al., 1990), the Total Ozone Mapping Spectrometer (TOMS) (Heath et al., 1975; McPeters et al., 1996) that was onboard NASA's Nimbus-7 satellite launched in October 1978, the Stratospheric Aerosol and Gas Experiment (SAGE) (McCormick et al., 1979, 1984), which was onboard the Applications Explorer Mission-2 (AME-2) satellite, SAGE-II (Mauldin et al., 1985), which was onboard the Earth Radiation Budget Satellite (ERBS), the ultraviolet spectrometer (UVS) that was onboard the Solar Mesosphere Explorer (SME) (Barth and Rusch, 1983; Solomon et al., 1983; Rusch et al., 1984) satellite that was launched in October, 1981 by NASA and the Global Ozone Monitoring Experiment (GOME) (Burrows et al., 1999), which was onboard the European Space Agency's (ESA) Second European Remote Sensing (ERS-2) satellite from April, 1995. The UVS onboard SME satellite was a limb spectrometer that observed the solar radiance that was scattered

*Corresponding author: GUO Xia, guoxia@mail.iap.ac.cn

in the Earth's atmosphere in the limb-viewing geometry, with a higher vertically resolved distribution of the atmospheric constituents and a wide spatial coverage as well.

During past few years, several new missions have been carried out that have contributed significantly to research in the fields of atmospheric chemistry and physics. The scanning imaging absorption spectrometer for atmospheric chartography (SCIAMACHY) (Bovensmann et al., 1999; von Savigny et al., 2002) is part of the atmospheric chemistry payload that was onboard ESA's Environmental Satellite (ENVISAT) that was launched in March, 2002. The SCIAMACHY instrument was designed to measure the sunlight transmitted, reflected and scattered by the Earth's atmosphere or surface in the wavelength region from 240–2380 nm and limb, nadir and occultation measurements were made during every orbit.

Similar to the SCIAMACHY instrument, the Optical Spectrograph and InfraRed Imaging System (OSIRIS) (Llewellyn et al., 1997; von Savigny et al., 2003), which was launched onboard the Swedish satellite ODIN in February of 2001, measures the scattered solar radiance in limb-viewing geometry over the spectral region from 280–800 nm. In addition, the atmospheric emission features (airglow) within the wavelength range of 280–800 nm and at particular wavelengths near 1270 nm and 1520 nm were intended to be measured by the OSIRIS instrument.

For the interpretation of satellite measurements, complex and precise radiation transfer models were required. Satellite measurements of the backscattered solar radiation in nadir-viewing geometry, as performed by SBUV, GOME and SCIAMACHY (nadir mode) could be accurately simulated using a pseudo-spherical/spherical radiative transfer model such as the discrete ordinate radiative transfer model (DISORT) (Stamnes et al., 1988) or the radiative transfer model for SCIAMACHY instrument (SCIATRAN) (Rozanov et al., 2001, 2002). However, the pseudo-spherical approximation is not accurate enough for large viewing and solar zenith angles (Caudill et al., 1997) in limb geometry. Thus, they are not appropriate for simulating limb measurements, such as those performed by SME, SCIAMACHY (limb mode) and OSIRIS. However, the accuracies of the radiative transfer models used in these studies have not been investigated or reported.

Therefore, for the interpretation of the limb measurements, a simple, fast and accurate radiative transfer model has been developed by the present authors, which takes into account the spherical atmosphere with an integration technique of self-adaptive variable space steps. Comparisons are carried out with the newly released radiative transfer model SCIATRAN2.0 and the SME measured limb-scattered ultraviolet radiation as well.

2. Radiative theory

The detector on the spacecraft views the atmospheric limb with an extremely small field of view and scans vertically along the tangent ray height as shown in Fig. 1.

The radiance scattered from the line of sight (LOS) can be comparative to a single-scattering radiative transfer algorithm in a spherically-layered atmosphere when the vertical distributions of the atmospheric parameters such as temperature, pressure, air density and trace constituents are known. It is assumed that the effects of the uncertainties at altitude of the spacecraft are negligible and that the effect of refraction along the LOS may also be ignored in the middle atmosphere, as the observations are executed from space. We assume that the atmosphere consists of only air molecules, ozone and aerosols, thus the Rayleigh scattering, ozone absorption and aerosol extinction are be taken into account. Other minor constituents that play a minimal role in the radiative transfer processes at ultraviolet wavelengths can be neglected.

The radiance seen by the ultraviolet spectrometer (UVS) is proportional to both the integral of number of scatterers along the LOS of the instrument and to the solar flux. For an optically-thin atmospheric layer with only Rayleigh scattering and ozone absorption, we are left with,

$$I_\lambda(z_0) = F_\lambda \sigma_\lambda \varphi(\phi) \int d\Omega \int_{-\infty}^{Sat} N[z(s)] \times \exp[-\tau_1(s) - \tau_2(s)] T_0(s) ds \quad (1)$$

where

$$\begin{cases} \tau_1(s) = \sigma_\lambda(\mathrm{O_3}) \int_s^{Sat} \mathrm{O_3}[z(s')] ds' \\ \tau_2(s) = \sigma_\lambda \int_s^{Sat} N[z(s')] ds' \end{cases} \quad (2)$$

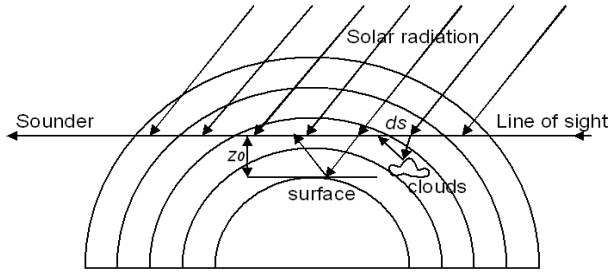

Fig. 1. Mapping of limb scanning geometry.

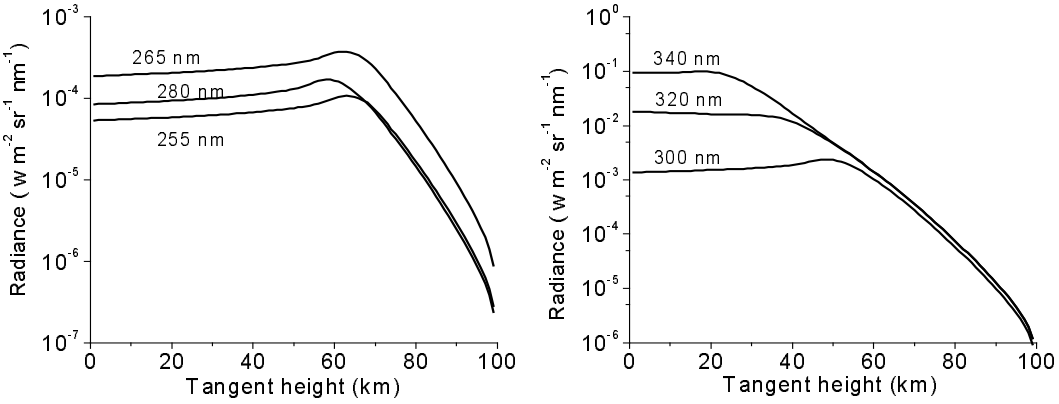

Fig. 2. Simulated radiances as a function of observational tangent ray height for each ultraviolet wavelength. The solar zenith angle is 45.0° and 1-km interval is assumed.

Here, z_0 is the tangent height, F_λ is the solar flux at wavelength λ, σ_λ is the Rayleigh scattering cross section, $\sigma_\lambda(O_3)$ is the ozone absorption cross section, $\varphi(\phi)$ is the Rayleigh phase function at the scattering angle ϕ and is normalized to unity when it is averaged over all scattering angles, $N[z(s)]$ is the the number density of air density at $z(s)$, $O_3[z(s)]$ is the ozone volume density, $\tau_1(s)$ is the optical depth of the ozone along the path from the scattering element ds to the satellite, $\tau_2(s)$ describes the loss over the same path due to Rayleigh scattering and $T_0(s)$ is the transmission of the solar radiation to the point of scattering ds. $I_\lambda(z_0)$ is the simulated total scattered radiance. The integral in Eq. (1) is performed along the LOS and over the field of view (Ω) of the instrument. The integrals in Eq. (2) are performed along the LOS from the scattering element ds up to the satellite.

When the extinction due to aerosol particles is considered, Eq. (1) becomes,

$$I_\lambda(z_0) = F_\lambda \int d\Omega \int_{-\infty}^{Sat} \{\sigma_\lambda \varphi(\phi) N[z(s)] + \sigma\omega P(\phi) N_a[z(s)]\} \exp[-\tau_1(s) - \tau_2(s) - \tau_a(s)] T_0(s) ds \quad (3)$$

where σ is the aerosol extinction cross section, ω is the aerosol single scattering albedo, $P(\phi)$ is the aerosol scattering phase function at a scattering angle of ϕ that is normalized to unity when it is averaged over all scattering angles, $N_a[z(s)]$ is the aerosol density at $z(s)$, and $\tau_a(s)$ is the optical depth of the aerosol along the path from the scattering element ds up to the satellite. For simplification, the parameters of the aerosol, such as the extinction cross section and the number density, are defined within an equivalent mono-disperse system.

To get the scattered radiance $I_\lambda(z_0)$ at the tangent height z_0 accurately and fast, a numerical integration method of height-dependent auto-adaptive modified space steps along the LOS was applied. First, the total optical length $\tau(s)$ along the LOS marked with tangent height z_0 is calculated. Secondly, a suitable $d\tau(s)$ is determined by inquiring in a look-up table, which is made in advance for all possible LOS with corresponding tangent heights in 1-km intervals. Thirdly, according to $d\tau(s)$, the auto-adaptive modified integral space step, ds, along the LOS is then determined, which assures that along the integral path the thicker the atmospheric air is, the shorter the space integral step. This integral method assures not only high accuracy, but also saves computation time.

3. Results and analysis

Suppose the satellite views the earth and atmosphere at a height of 534 km above sea level, which is the average altitude of the SME satellite. We consider radiative processes of Rayleigh scattering, ozone absorption and aerosol extinction, while ignore multiple scattering events. Here, the winter middle-latitude standard atmosphere developed by the Air Force Geophysics Laboratory (AFGL) with a top of 120 km and the autumn/winter rural aerosol are adopted. The surface visibility was about 23 km and the background stratosphere aerosol was chosen.

Figure 2 shows the vertical distributions of the modeled radiances at different ultraviolet wavelengths, where the solar zenith angle is set to 45.0°, and the measurement azimuth angle comparative to the sun is set to 0.0°.

Figure 2 indicates that the scattered radiance profiles at all ultraviolet wavelengths complied with a similar law, that is, at high altitudes, where the absorption by ozone was small, the radiance increased exponentially with decreasing altitude and then reached a region where the ozone absorption becomes significant

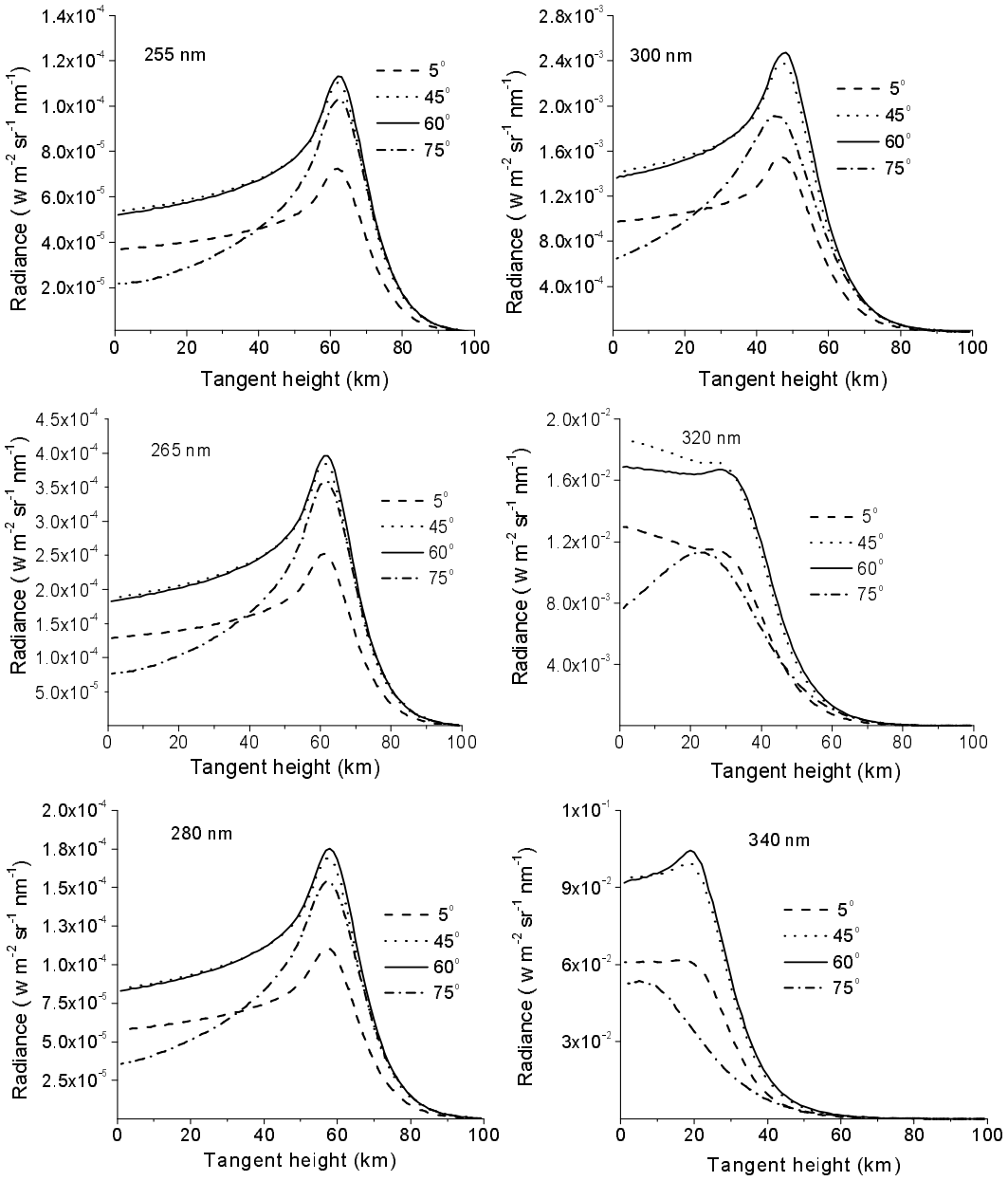

Fig. 3. Simulated radiances as a function of observational tangent ray height in the ultraviolet band for solar zenith angles of 5.0°, 45.0°, 60.0° and 75.0°. 1-km interval is assumed.

and the exponential increase in the radiance was modified. When the optical depth of the ozone along the LOS approached unity, the radiance came to a head, thereafter decreasing gradually below. However, for longer wavelengths, such as 320 nm, the value may keep increasing down into the lower atmospheric layers, where an increased radiance due to the increased scatterers, makes it possible to bypass the attenuation along this long path. Generally, the altitude with the maximum observed radiance moves downward with increasing wavelength and for wavelengths smaller than 300 nm, it is typically located at about 50–65 km in the lower mesosphere, while for wavelengths longer than 300 nm, it is typically found in the middle stratospheric region. The altitude of the maximum radiance is heavily wavelength dependent, as well as being dependent upon the ozone cross section and the integrated number of ozone molecules and it changes minimally with the different seasons or regions for a specified wavelength.

Figure 3 presents the vertical distributions of the modeled radiance at different ultraviolet wavelengths

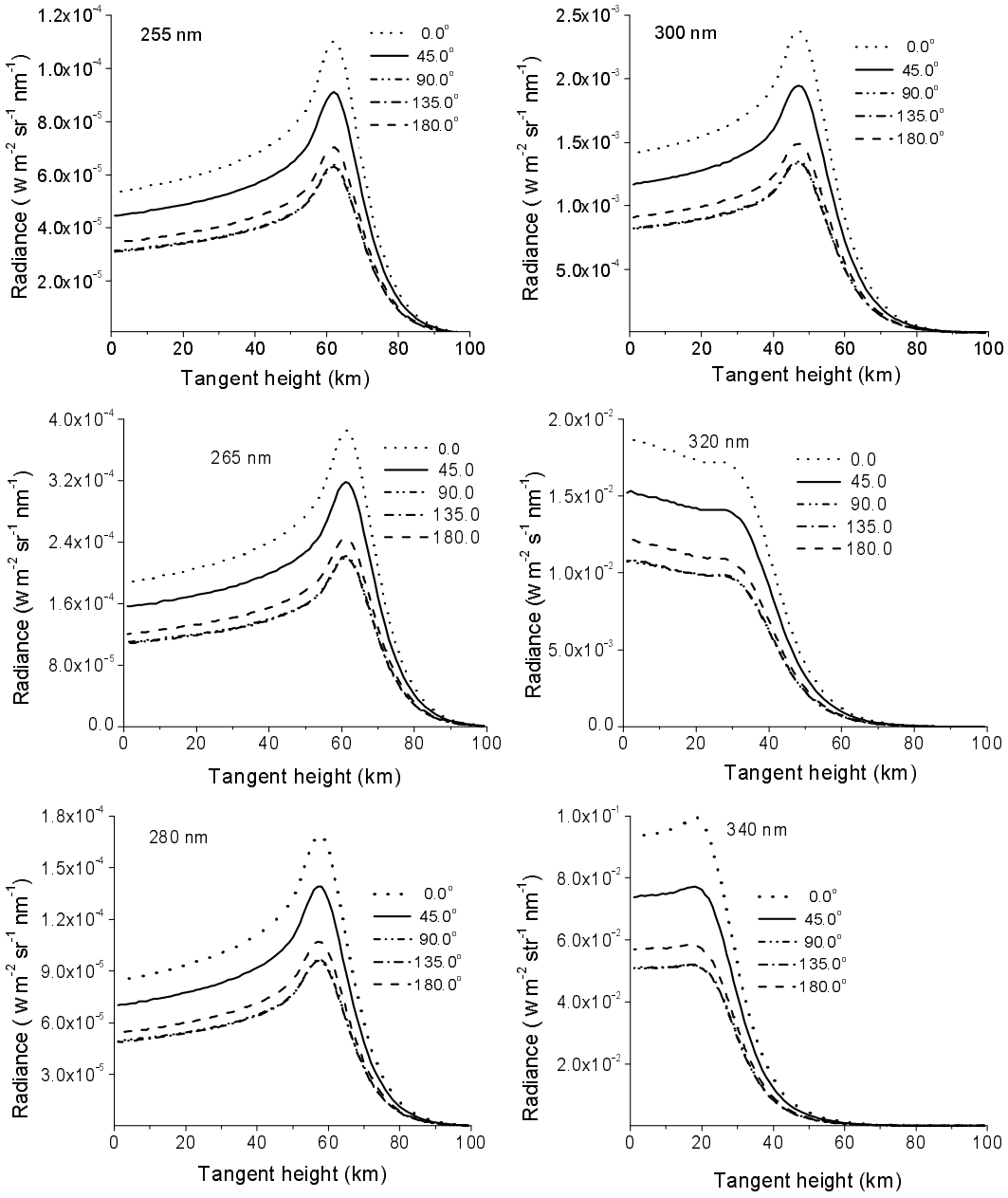

Fig. 4. Simulated radiances as a function of observational tangent ray height in the ultraviolet band for measurement azimuth angles relative to the sun of 0.0°, 45.0°, 90.0°, 135.0° and 180.0°. 1-km interval is assumed.

where the azimuth angle of the measurement relative to the sun is 0.0° and the solar zenith angle is 5.0°, 45.0°, 60.0° and 75.0°, respectively, and the other parameter setting is the same as in Fig. 2.

It is clearly seen that at wavelengths below 300 nm, except the 75.0° radiance profile, the scattered radiance increased with increasing solar zenith angle, but for the 60.0° profile, which below the height of the maximum radiance, drops as the height is decreased slightly faster than that for the 45.0° profile. When the solar zenith angle is 75.0° below the height of maximum radiance, the radiance decreased with decreased height more rapidly and became much lower than the other profiles in the lower layers. For wavelengths of 320 nm and 340 nm at larger solar zenith angles such as 60.0° and 75.0°, the radiance decreases more in the middle and lower layers, especially for the 75.0° radiance profiles, since the sun lowers in the sky, the beam path of the light through the air to the scattering unit becomes much longer, thereby greatly diminishing the

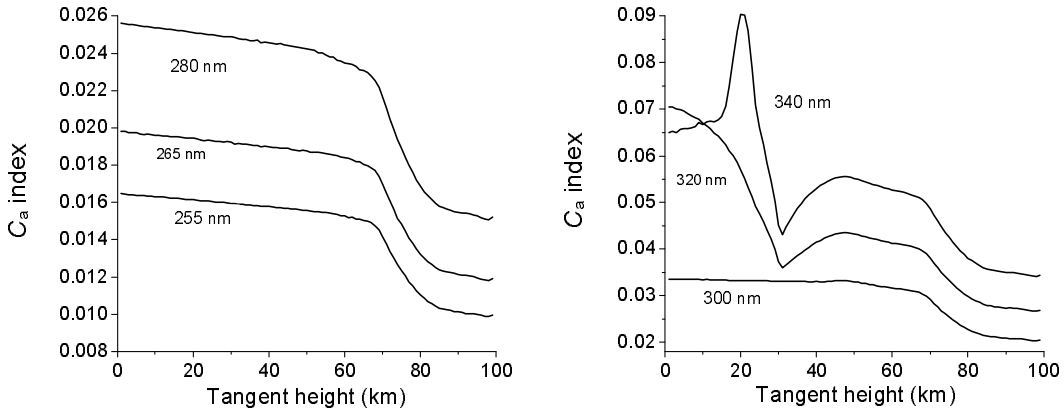

Fig. 5. Vertical distributions of modeled C_a index at each ultraviolet wavelength in the same condition as in Fig. 2.

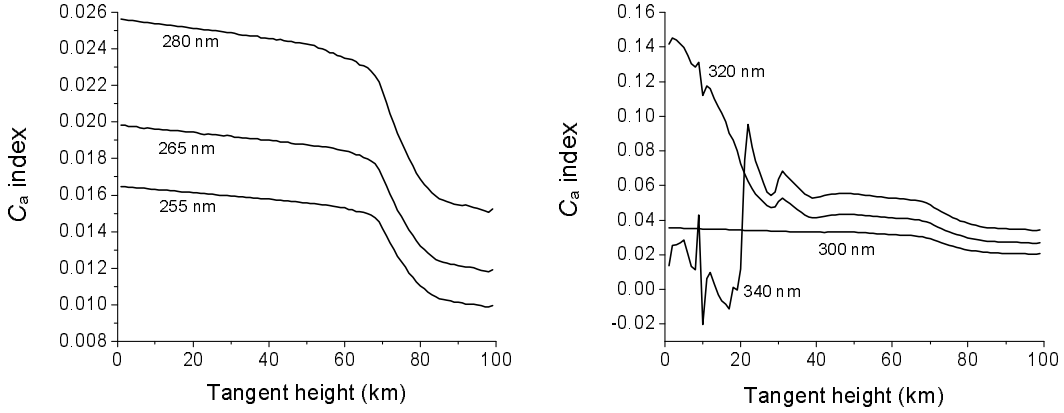

Fig. 6. Vertical distributions of modeled C_a index at each ultraviolet wavelength with strong stratospheric aerosol and a surface visibility of 5 km.

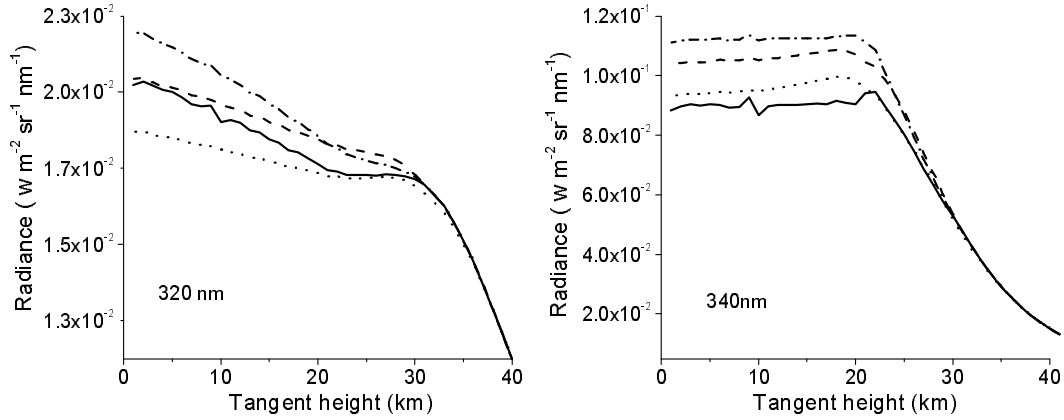

Fig. 7. Modeled vertical radiance distributions at four different stratospheric aerosol types as background (dotted line), moderate (dashed line), high (dash-dotted line) and extreme (black line) volcanic aerosols respectively. The atmospheric structure and model parameter setting is the same as in Fig. 2.

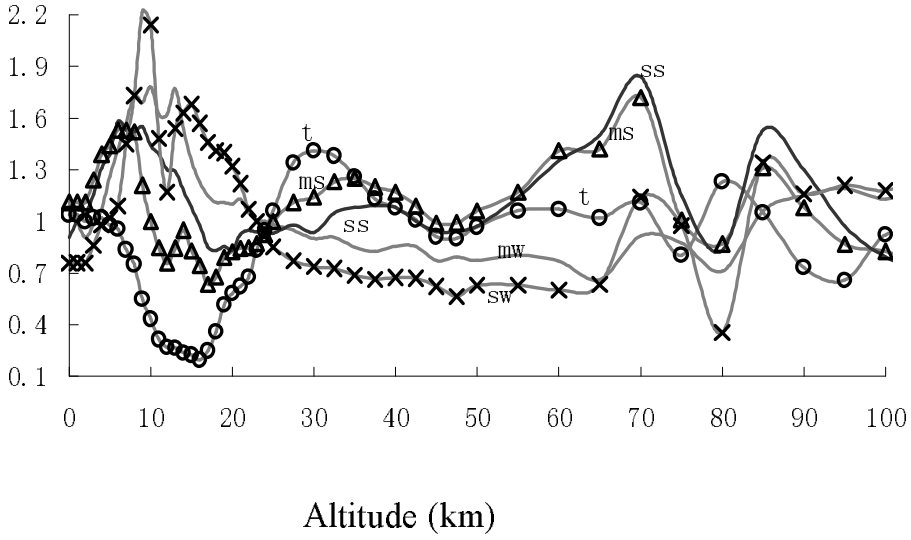

Fig. 8. AFGL standard ozone vertical distributions. The x-axis is altitude (km) and the y-axis is the ratio of the other number densities to the AFGL U. S. standard ozone distributions. The black line is for sub-arctic summer (ss), the gray line for mid-latitude winter (mw), the gray line with circles for tropics (t), the gray line with triangles for mid-latitude summer (ms) and the gray line with crosses for sub-arctic winter (sw).

Table 1. Range of $C_{\rm a}$ value for each wavelength.

λ	255 nm	265 nm	280 nm	300 nm	320 nm	340 nm
$C_{\rm a}$	0. 01∼0. 016	0. 013∼0. 019	0. 016∼0. 026	0. 02∼0. 035	0. 03∼0. 07	0.04∼0.09

solar flux and the scattered radiance measured by the instrument.

Figure 4 shows the vertical distribution of the modeled radiance for different ultraviolet wavelengths, where the solar zenith angle is 45.0° and the measurement azimuth angles relative to the sun are 0.0°, 45.0°, 90.0°, 135.0° and 180.0°. In this case, when the measurement azimuth angle relative to the sun was 0.0°, the scattered radiance was the largest. When the measurement azimuth angle relative to the sun was either 90.0° or 135.0°, the scattered radiance became relatively smaller. Obviously, the scattered radiation causes dramatic changes, due to the changeable measurement angles for a specific solar zenith angle. This is because the Rayleigh scattering and the two term Heyney-Greenstein (H–G) aerosol phase function, that are associated with the limb-scattered radiations (seen in Eq. 3), are functions of the scattering angle , which depends both on the solar zenith angle and the measurement angle.

Aerosols play an important role in the radiative transfer processes in the earth-atmospheric system mainly through the strong scattering effect in the ultraviolet band. For quantitatively estimating the contribution to the total radiance due to aerosol particles, we define an index $C_{\rm a}$, as shown below,

$$C_{\rm a} = (I_{\rm a} - I)/I_{\rm a} \tag{4}$$

where $I_{\rm a}$ and I are the modeled radiances with and without including the influence of aerosol. Figure 5 provides the vertical distributions of $C_{\rm a}$ for several ultraviolet wavelengths with a similar parameter setting as in Fig. 2.

From Fig. 5 we can see that, in general, the aerosol index, $C_{\rm a}$, increases with increasing wavelength and decreases with increasing ray tangent height. For longer wavelengths, such as 320 nm and 340 nm, $C_{\rm a}$ takes on unique characteristics in the stratosphere, that is, for 320 nm, it increases very fast with decreasing height and reaches maximum of 0.07 at the ground and for 340 nm, it reaches maximum of 0.09 at about 20 km, then decreases dramatically with decreasing height. This is due to increased number density of aerosol particles in the lower atmosphere, which causes the extinct radiation may counteract or even exceed the increased radiation due to strengthened aerosol particles. Table 1 shows the value range of $C_{\rm a}$

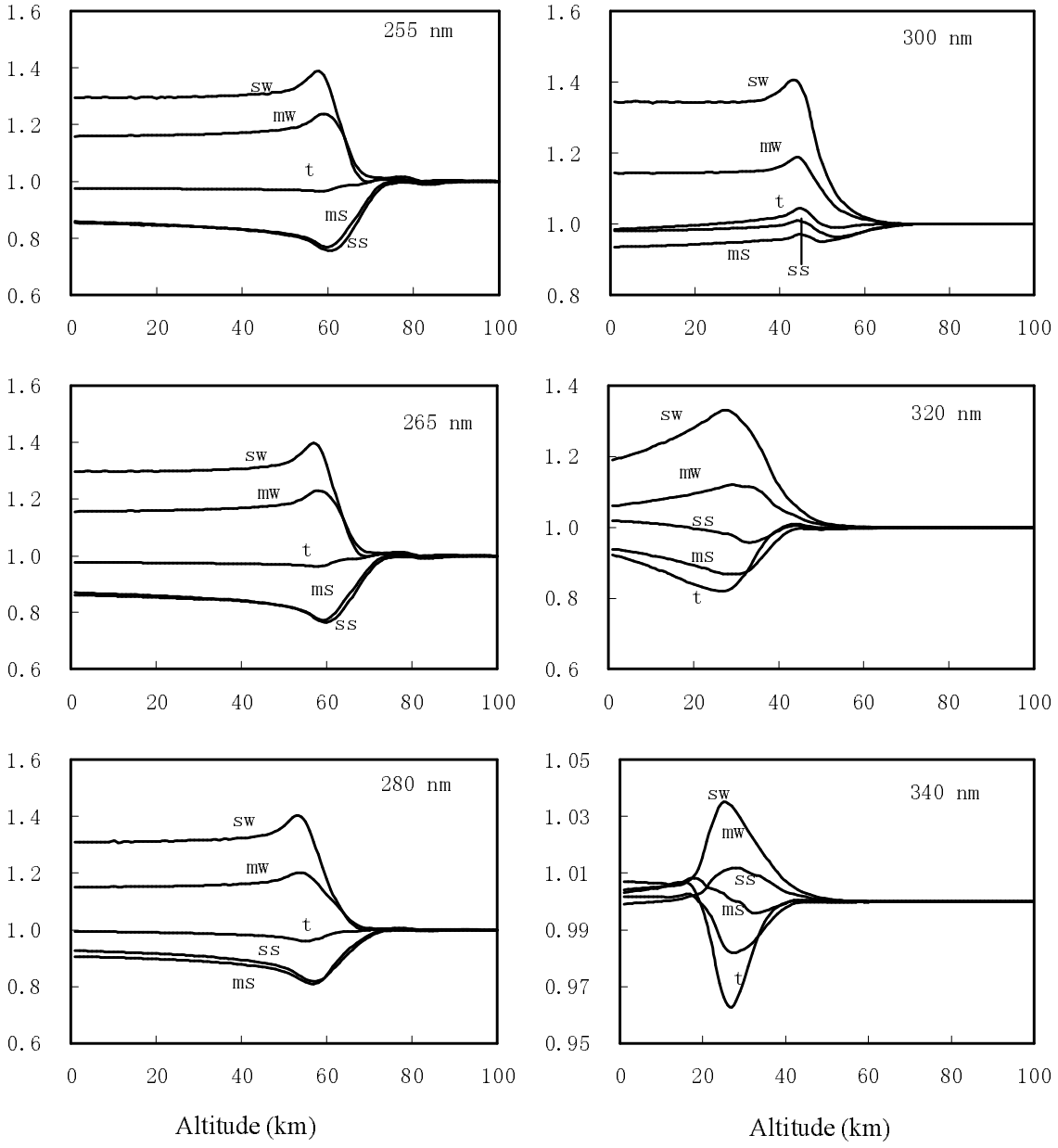

Fig. 9. The modeled limb-scattered radiations with different ozone distributions according to Fig. 8. The x-axis is altitude (km) and the y-axis is the ratio of the other modeled radiances to the modeled radiance with the AFGL U.S. standard ozone distribution.

for each wavelength.

Obviously, the contribution of the aerosol particles to the total radiance is not significant over the entire ultraviolet waveband, most especially for shorter wavelengths. When the wavelength is shorter than 300 nm, C_a is typically no more than 3% in the atmospheric layer. For wavelengths longer than 300 nm, C_a is larger in the lower stratosphere, up to 9%, and in the upper regions the maximum of C_a is measured to be less than 4.2% at 320 nm and 5.5% at 340 nm.

Figure 6 shows the corresponding C_a index vertical distributions for several ultraviolet wavelength when a surface visibility of 5 km and a stratospheric high volcano aerosol were adopted. This indicates that for shorter wavelengths, radiative contributions due to increased stratospheric and tropospheric aerosols, stays relatively small, while it is greatly enhanced at longer wavelengths. For a wavelength of 320 nm, in the lower atmosphere, C_a grows very rapid with decreasing height up to 14.5% and for 340 nm, C_a index even becomes negative, which indicates that the attenuation effect along the long path has become dominant

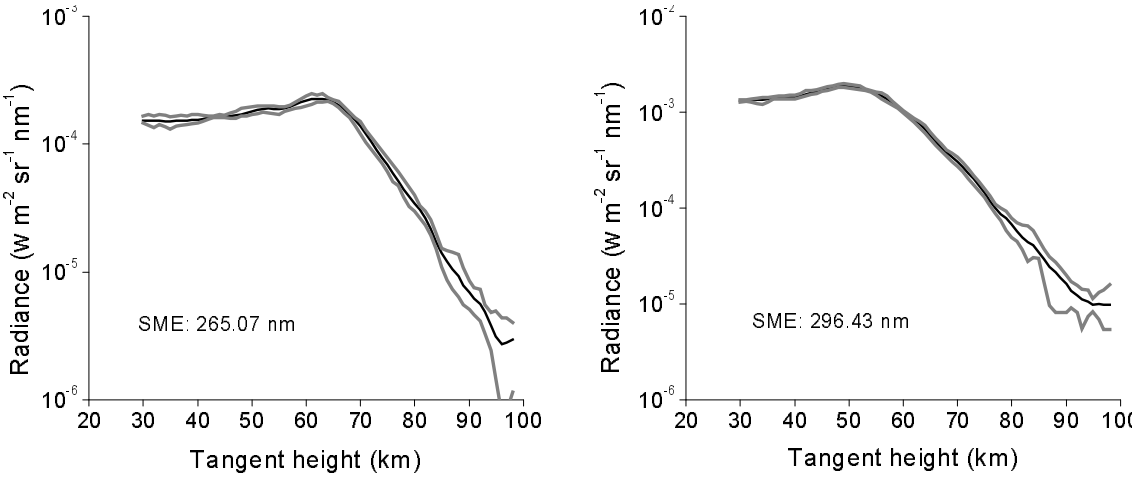

Fig. 10. Radiance profiles from record 21 on the orbit of 1059 on 15 December 1981. The black line is the average of the 6 successive spins used for this record and the gray lines are the dynamic range of the radiance for the six successive spins.

due to the larger aerosol loading.

Scattered earth radiances of different stratosphereic types of aerosols, being either background, moderate, high or extreme volcanic aerosols, are modeled (see Fig. 7). Since radiances for ultraviolet wavelengths shorter than 300 nm are not significantly influenced by varying stratospheric types of aerosols, we modeled the radiances only at the longer wavelengths, 320 and 340 nm.

For the limb geometry, the scattered radiance at a certain tangent height, z_0, is mainly contributed due to the atmospheric layer around z_0 and above, so aerosol changes in the stratosphere have little effects on radiance above it. Therefore, radiances below the stratosphere are only mapped in Fig. 7. This map, which again manifests that aerosol's contribution to the measured scattered radiances may be negative for the longer ultraviolet wavelengths due to the strengthened aerosol concentration.

Besides aerosols, ozone also plays a key role in the radiative transfer process through the strong absorption extinction in the Hartley and Huggins bands. Following the AFGL ozone vertical-distributions are presented in Fig. 8.

From the above, we can see that the ozone average vertical-distributions have large variances dependent upon both the season and changing latitude. In the lower stratosphere around an altitude of 16 km, the ozone concentration in winter in the sub-arctic region is nearly up to 6 times that in the tropical region. The corresponding modeled limb radiances with different ozone distributions are illustrated in Fig. 9.

Based on the above, one can see that, generally speaking, relative variances in the scattered radiance dramatically change correspondingly with the variable ozone distributions due to the ozone absorption extinction. For short wavelengths (no more than 300 nm), the region sensitive to ozone radiation are from above the upper stratosphere to the middle mesosphere, which greatly determines scattered radiances. Therefore, scattered radiances changed due to the variable ozone in this region, where the richer the ozone was, the weaker the scattered radiance became, as is seen in Fig. 9. For longer wavelengths, such as 320 nm and 340 nm, which have relatively weaker absorption coefficients, the scattered radiations are more sensitive within the altitude range of 20–40 km and thus similar results are obtained here.

It is noticeable that variances in the ozone within the upper atmosphere have no apparent effects on the scattered radiance, even at short ultraviolet wavelengths. This is due to the fact that ozone is fairly sparse within the upper atmosphere and the ozone absorption extinction is less significant when compared with the reductions induced by ozone in the lower atmosphere.

4. Comparison

For further verification of the precision of the simulation by using the present model for the ultraviolet limb scanning radiative-transfer problem, here the measurements from the UVS instrument onboard the SME satellite along with the modeled radiances from the newly released SCIATRAN2.0 spherical model were applied to carry out this study.

The SME satellite was launched in October, 1981.

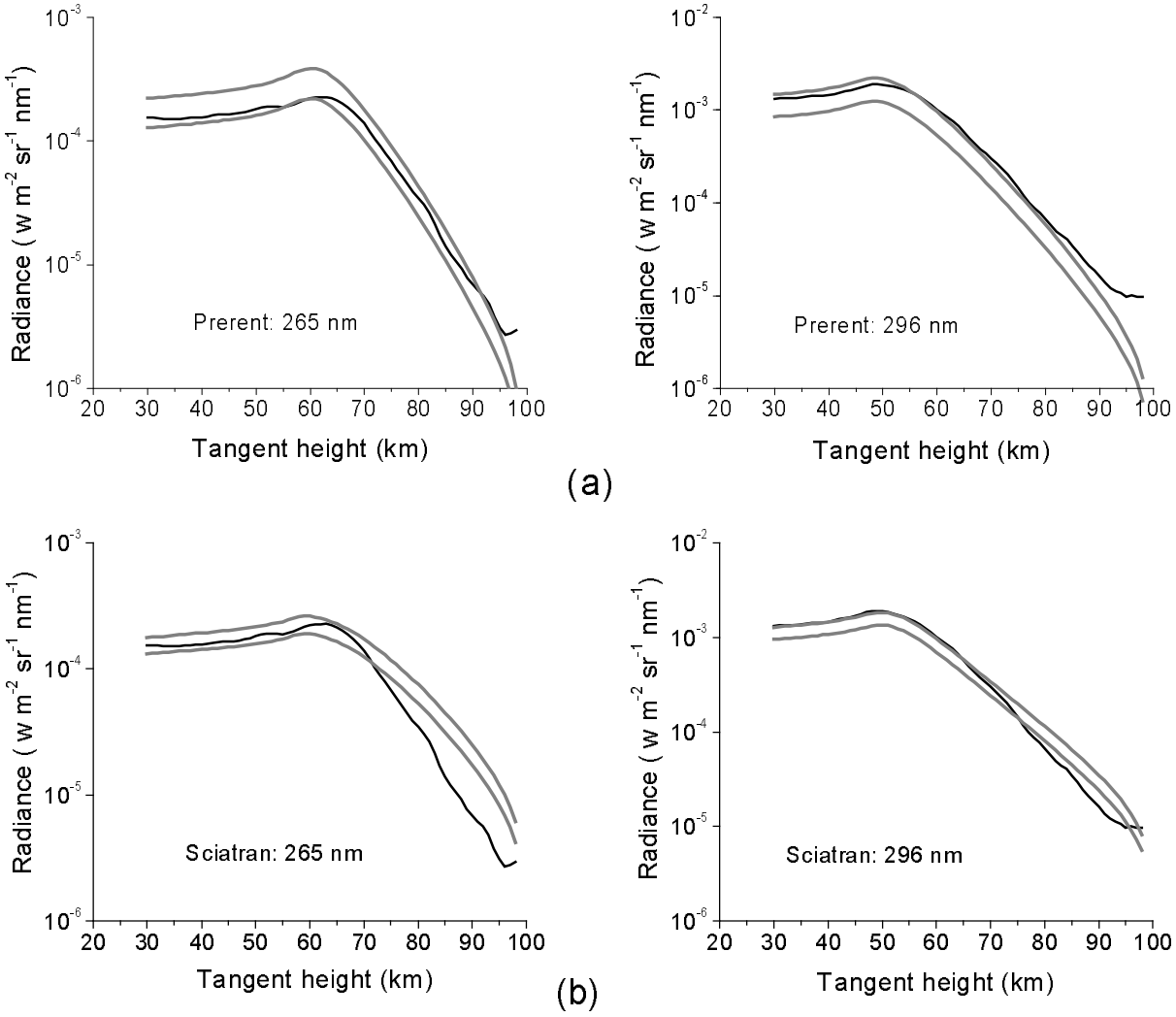

Fig. 11. Comparison of modeled radiances with the SME-measured radiance at two ultraviolet wavelengths. (a) for the present model; (b) for the SCIATRAN2.0 model. The black line is SME-measured average radiance and the two gray lines are modeled maximum and minimum radiance profiles at a solar zenith angle of 45°.

It was in a circular, sun-synchronous, near-polar orbit, with a mean altitude of 534 km, together with its ascending node at near 1500 LST. The SME satellite was designed to measure ozone, water vapor and temperature in the atmosphere, along with the relevant solar flux, in order to test the photochemical theories of ozone in the earth's mesosphere. The UVS instrument was designed to measure the altitude profiles of the Rayleigh-scattered solar photons in the 200–340 nm spectral region. The satellite is spin stabilized at 5 rpm and scans the atmosphere at the earth's leading (or trailing) limb during each spin period. During each of the earth's limb, 32 data samples are recorded on two separate channels on timescales of 2 ms and 44 ms per sample, respectively, with an altitude interval varying from about 100 km to 0 km being sampled on each spin. The satellite moved approximately 0.75° along its orbit during each spin period and the measured scattered radiance data collected every six consecutive spins were packed into one record, thus, providing a latitude resolution of about 5° for a polar-orbiting satellite by averaging these six consecutive spins. One record of the altitude-dependent and spatially-coincident radiance profile collected over the two channels (296.43 nm and 265.07 nm) is illustrated in Fig. 10, which was scanned during the orbit of 1059 on 15 December 1981, over the winter southern-middle latitude region (about 45.0°), with a solar zenith angle of 45.0° and a scattering angle of 80.0°. The black line in Fig. 10 refers to the average vertical distributions of these 6 successive spins and the two gray lines to the dynamic range of the radiance for these six successive spins in the record.

From Fig. 10, one can see that the measured ra-

diance profile complies with a similar dependence as the modeled one. We notice that in Fig. 10, there are many random fluctuations in the measured radiances for the records of both 296.43 nm and 265.07 nm, similar to that which is caused by the instantaneous spatial and temporal variations within the atmosphere, sensitivity of the instrument, along with the signal disposal, data receiving and processing errors. The measured radiances for the two channels, 265.07 nm and 296.43 nm, are comparable with the modeled radiances for 265 nm and 296 nm that are simulated by the present model and the recently released, spherical-layered model SCIATRAN2.0 (Rozanov et al., 2001; Rozanov et al., 2002).

Figure 11 provides the modeled and SME-measured radiances. In these two sub-figures, the black line displays the SME measured average radiances as the same in Fig. 10 and the two gray lines are associated with the modeled maximum and minimum radiances among all measurement relative azimuth angles from 0° to 180° in reference to the sun, with a solar zenith angle of 45°, thus, generally assuring a similar atmosphere circumstance and sunshine for the measured and modeled radiances. Other parameters are the same as those depicted in Fig. 2.

From Fig. 11a, one can see that the measured radiance profiles from the measurements and the present model, for 265 nm and 296 nm, respectively, were nearly the same both in profile shape and magnitude. A maximum in the modeled radiance are observed at about 62 km for 265 nm and 48 km for 296 nm. For the tangent height, the measured and modeled profiles coincided fairly well, except within the upper mesosphere and lower thermosphere (from 80 to 100 km), where there are comparatively large deviations for the larger wavelength (296 nm). For the case of SCIATRAN2.0 (see Fig. 11b), the measured and modeled profiles coincided fairly well below 70 km, however, there are larger deviations existing over both channels than those presented in Fig. 11a in the upper atmosphere, where the former was lower than the latter. From the above figures, it has been shown that the radiance modeled by the present model was more coincident with the measured values on these two channels and had better accuracy than the SCIATRAN2.0 model, especially in the region between 70 km and 100 km.

5. Conclusions

In the present paper, the authors have developed a simple and fast ultraviolet-limb scanning-radative transfer model in the spherical planetary atmosphere with an auto-adaptive, modified space-step integration method and carried out research on ultraviolet radiative spectral characteristics for varying solar zenith angles and measurement azimuth angles. The radiative effects for the different aerosol and ozone structures are also examined. In the end, preliminary comparisons with SME measured and SCIATRAN2.0 modeled radiances in the 20–100 km region, have been completed for the two short ultraviolet wavelengths at 265 nm and 296 nm.

We can conclude that the present spherical model based on the single-scattering approximation is suitable for describing the ultraviolet limb scanning radiative transfer process and has considerable accuracy in the height range from the mid-stratosphere up to the entire mesosphere. Furthermore, these multiple scattering and aerosol radiative effects need to be correctly considered when studying the lower stratospheric and tropospheric atmosphere. This work will be helpful for providing an improved method for surveying the constitution of the middle atmosphere (Guo et al., 2004) and for understanding the radiative, chemical and dynamical processes that occur, and thus, their impact on both the lower and upper atmosphere.

Acknowledgements. This work was supported by National Natural Science Foundation of China (NSFC) under Grant Nos. 40333034 and 40504022. The SME-measured data were kindly provided by Dr. D. W. Rusch of University of Colorado.

REFERENCES

Barth, C. A., and D. W. Rusch, 1983: Solar mesosphere explore: scientific objectives and results. *Geophys. Res. Lett.*, **10**, 237–240.

Bovensmann, H., J. P. Burrows, M. Buchwitz, J. Frerick, S. Noñl, V. V. Rozanov, K. V. Chance, and A. P. H. Goede, 1999: SCIAMACHY: Mission objectives and measurement modes. *J. Atmos. Sci.*, **56**, 127–150.

Burrows, J. P., and Coauthors, 1999: The Global Ozone Monitoring Experiment (GOME): Mission concept and first scientific results. *J. Atmos. Sci.*, **56**, 151–175.

Caudill, T. R., D. E. Flittner, B. M. Herman, O. Torres, and R. D. McPeters, 1997: Evaluation of the pseudo-spherical approximation for backscattered ultraviolet radiances and ozone retrieval. *J. Geophys. Res.*, **102**, 3881–3890.

Fleig, A. J., R. D. McPeters, P. K. Bhartia, B. M. Schlesinger, R. P. Cebula, K. F. Klenk, S. L. Taylor, and D. F. Heath, 1990: Nimbus 7 Solar Backscatter Ultraviolet (SBUV) ozone products user's guide. NASA Ref. Pub., 1234.

Guo, X., Y. Lü and D. Lü, 2004: Feasibility study for retrieval of air density and ozone concentration profiles in the mesosphere using an ultraviolet limb-scan

technique. *Progress in Natural Science*, **14**, 504–510.

Heath, D. F. , A. J. Krueger, H. A. Roeder, and D. B. Henderson, 1975: The solar backscatter ultraviolet and total ozone mapping spectrometer (SBUV/TOMS) for NIMBUSG. *Optical Engineering*, **14**, 323–331.

Llewellyn, and Coauthors, 1997: OSIRIS—An Application of Tomography for Absorbed Emissions in remote Sensing. *Applications of Photonic Technology*, **2**, 627–632.

Mauldin, L. E. III, N. H. Zaun, M. P. McCormick, J. L. H. Guy, and W. R. Vaughn, 1985: Stratospheric Aerosol and Gas Experiment II instrument: A functional description. *Optical Engineering*, **24**, 112–117.

McCormick, M. P., P. Hamill, T. J. Pepin, W. P. Chu, T. J. Swissler, and L. R. McMaster, 1979: Satellite studies of the stratospheric aerosol. *Bull. Amer. Meteor. Soc.*, **9**, 1038–1046.

McCormick, M. P., T. J. Swissler, E. Hilsenrath, A. J. Krueger, and M. T. Osborn, 1984: Satellite and correlative measurements of stratospheric ozone: Comparison of measurements made by SAGE, ECC Balloons, chemiluminescent, and optical rocketsondes. *J. Geophys. Res.*, **89**, 5135–5320.

McPeters, R. D., and Coauthors, 1996: Nimbus-7 Total Ozone Mapping Spectrometer (TOMS) data products user's guide. NASA Ref. Pub., 1384.

Müller, R., P. J. Crutzen, J. U. Groob, C. Brühl, J. M. Russel III, H. Gernandt, D. S. McKenna, and A. F. Tuck, 1997: Severe chemical ozone loss in the Arctic during the winter of 1995–1996. *Nature*, **398**, 709–712.

Newman, P. A., J. F. Gleason, R. D. McPeters, and R. S. Stolarski, 1997: Anomalously low ozone over the Arctic. *Geophys. Res. Lett.*, **24**, 2689–2692.

Rozanov, A., V. Rozanov, and J. P. Burrows, 2001: A numerical radiative-transfer model for a spherical planetary atmosphere: Combined differential-integral approach involving the Picard interative approximation. *Journal of Quatitative Spectroscopy and Radiative Transfer*, **69**, 491–512

Rozanov, V. V., M. Buchwitz, K. -U. Eichmann, R. de Beek, and J. P. Burrows, 2002: SCIATRAN—A new radiative-transfer model for geophysical applications in the 240–2400 nm spectral region: The pseudo-spherical version. *Advances in Space Research*, **29**, 1831–1835.

Rusch, D. W. , G. H., Mount, C. A., Barth, R. J., Thomas, and M. T. Callan, 1984: Solar mesosphere explorer ultraviolet spectrometer: Measurements of ozone in the 1. 0–1. 0 mbar region. *J. Geophys. Res.*, **89**, 11677–11687.

Solomon, S., D. W., Rusch, R. J., Thomas, and R. S., Echman, 1983: Comparison of mesospheric ozone abundances measured by the solar mesosphere explorer and model calculations. *Geophys. Res. Lett.*, **10**, 249–252.

Stamnes, K., S. C. Tsay, W. Wiscombe, K. Jayaweera, 1988: Numerically stable algorithm for discrete-ordinate-method radiative transfer in multiple scattering and emitting layered media. *Applied Optics*, **27**, 2502–2509.

von Savigny, C. , A. Rozanov, K.-U. Eichmann, V. Rozanov, H. Bovensmann, and J. P. Burrows, 2002: First SCIAMACHY limb results. *1st German SCIAMACHY/GOME Meeting*, Bremen, 25–26 November.

von Savigny, C., and Coauthors, 2003: Retrieval of stratospheric ozone density profiles retrieved from limb scattered sunlight radiance spectra measured by the OSIRIS instrument on the Odin satellite. *Geophys. Res. Lett.*, **30**, 1755–1758.